Hydrodynamics of a semipermeable inextensible membrane under flow and confinement

Bryan Quaife,[1] Ashley Gannon,[1] and Y.-N. Young[2,*]

[1]*Department of Scientific Computing, Florida State University, Tallahassee, Florida 32306, USA*

[2]*Department of Mathematical Sciences, New Jersey Institute of Technology, Newark, New Jersey 07102, USA*

(Received 17 February 2021; accepted 15 June 2021; published 6 July 2021)

Lipid bilayer membranes have a native (albeit small) permeability for water molecules. Under an external load, provided that the bilayer structure stays intact and does not suffer from poration or rupture, a lipid membrane deforms and its water influx/efflux is often assumed negligible in the absence of osmolarity. In this work we use boundary integral simulations to investigate the effects of water permeability on the hydrodynamics of an inextensible membrane under a mechanical load, such as the viscous stress from an external flow deforming an inextensible membrane in free space or pushing it through a confinement. Incorporating the membrane permeability into the framework of Helfrich free energy for an inextensible, elastic membrane (a vesicle), we illustrate that, in the absence of an osmotic stress gradient, the semipermeable vesicle is affected by water influx/efflux over a sufficiently long time or under a strong confinement. Our simulations quantify the conditions for water permeation to be negligible in terms of the timescales, flow strength, and confinement. These results shed light on how microfluidic confinement can be utilized to estimate membrane permeability.

DOI: 10.1103/PhysRevFluids.6.073601

I. INTRODUCTION

Water exchange is essential for a living cell to adapt to its environment over a wide range of timescales [1–9]. Recent findings confirm that both osmotic and mechanical stresses contribute to significant water permeation for cells to migrate under strong confinement [10–13], leading to a dynamic surface-to-volume ratio of a migrating cell. While stress-induced release of messengers in cells has been well studied [14–18], mechanically induced water permeation is often associated with membrane poration or rupture under extreme stresses [19,20].

The cellular membrane is a lipid bilayer membrane that is slightly permeable to water and lipid-soluble molecules [21–24]. In the red blood cell membrane, aquaporin-1 channels give rise to a much higher water permeability coefficient of approximately 1.8×10^{-2} cm/s in erythrocytes [3] while the intrinsic water permeability of a lipid bilayer membrane is in the range of 10^{-4}–10^{-3} cm/s [22,24–27]. Without aquaporins or other membrane channels to promote water permeability, the intrinsic membrane permeability is known to depend on the temperature, lipid composition [28], and the hydration of the membrane [29]. Molecular dynamic simulations show that a stretched red blood cell membrane porates when the membrane tension reaches the order of 2–4 mN/m, giving rise to membrane rupture and leakage of macromolecules (see Razizadeh *et al.* [20] and references therein). Consequently, as long as the lipid bilayer membrane remains intact (no poration or rupture), the total amount of water inside the membrane is assumed constant throughout the experiment of duration no longer than tens of minutes.

*Corresponding author: yyoung@njit.edu

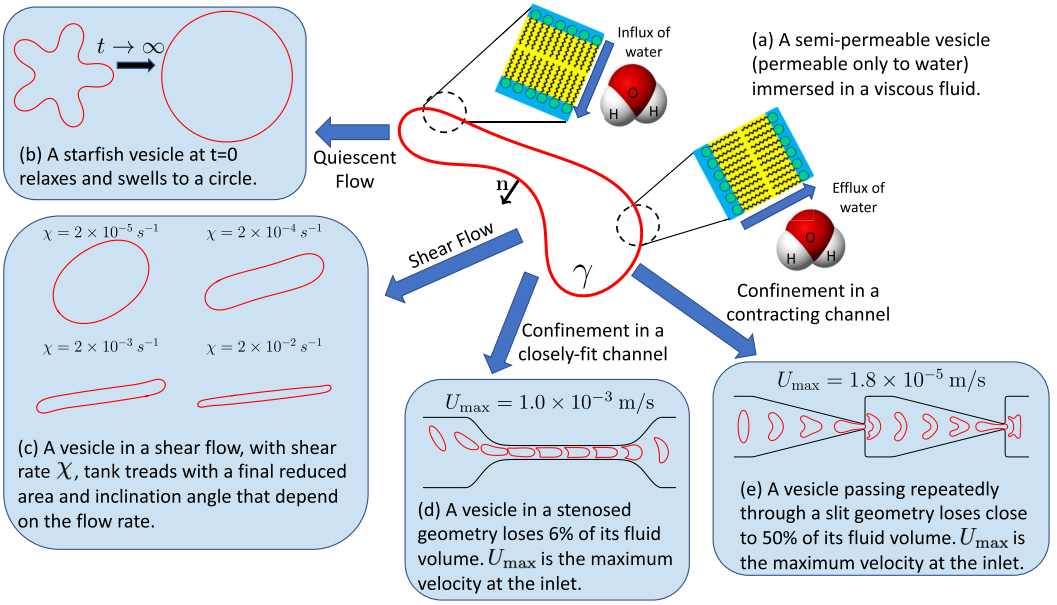

FIG. 1. Schematics showing the effects of semipermeability on vesicle hydrodynamics in various configurations. The lipid bilayer membrane (modeled as an interface γ of zero thickness and an outward normal $\mathbf{n}$) is permeable to water molecules, depending on the mechanical normal stress balance on the membrane. The slipper in (a) is the steady-state shape of a semipermeable vesicle in a Poiseuille flow.

Vesicles are self-enclosed lipid bilayer membranes (often without transmembrane proteins), and they have been used as a model system to study reshaping, remodeling, and scission of cell membranes due to osmotic stress [26,27,30–32]. In most modeling works of vesicle hydrodynamics in free space, the permeating water flow due to a jump in hydrodynamic pressure is neglected (e.g., see Vogl *et al.* [33]). Recent results illustrate that the permeating water flow is inevitably coupled with the mechanical pressure jump across the membrane [13], which could become comparable to osmotic stress when the membrane deformation is large under confinement [12,13]. Motivated by these results we extend the Helfrich free energy for an inextensilbe elastic vesicle membrane to incorporate membrane permeability for the viscous solvent (water) to study the hydrodynamics of such semipermeable membrane.

In this work we use modeling and direct numerical simulations to show that, over the appropriate timescales or under strong confinement, the intrinsic membrane permeability to water can give rise to significantly distinct hydrodynamics of a semipermeable vesicle. In microfluidic experiments, it is challenging to keep a freely suspended red blood cell or vesicle in a steady flow for more than a few hours. It is also difficult to quantify the vesicle surface-to-volume ratio accurately [34]. Using our model and integral simulations, we aim to address the following questions: Under what flowing conditions can we assume that vesicle conserves its water content? Do liposomes conserve volume under flow over a long time (hours)? What is the dynamic consequence when water influx/efflux affects the membrane hydrodynamics?

To answer these questions, we focus on the balance between hydrodynamics stresses, tension, and elastic stress of a semipermeable membrane under various flowing conditions and confinement (Fig. 1). Using numerical simulations described in Sec. II and Sec. III we quantify the effects of water permeability on the hydrodynamics of a vesicle under mechanical stresses. Without an osmotic gradient, we first show that a freely suspended semipermeable vesicle behaves differently from an impermeable vesicle over a long time in Sec. IV. Next in Sec. V we show that the permeating water flow can be amplified by extreme confinement to give rise to observable change

in both vesicle hydrodynamics and vesicle's water content. These results provide insight into quantifying the effects of membrane permeability on vesicle hydrodynamics in microfluidics.

II. FORMULATION

We consider a two-dimensional semipermeable vesicle (permeable only to water) suspended in a viscous fluid (Fig. 1), and we let γ denote the membrane boundary, of length L and enclosing a region of area A. To focus on the effect of water flow on vesicle hydrodynamics in various conditions, we assume the fluid is the same inside and outside the vesicle membrane. On the membrane the permeable water flux gives rise to a difference between the fluid velocity $\mathbf{u}(\mathbf{x} \in \gamma)$ and the membrane velocity $\dot{\mathbf{x}}$ [13]:

$$\mathbf{u} - \dot{\mathbf{x}} = -k_w(RT\triangle c + \mathbf{f}_{\text{mem}} \cdot \mathbf{n})\mathbf{n}, \qquad \mathbf{x} \in \gamma, \tag{1}$$

where $\mathbf{n}$ is the outward normal (Fig. 1), k_w is the hydraulic conductivity ($\text{m}^2\text{s/kg}$), R is the ideal gas constant, T is the temperature (K), $\triangle c$ is contrast in a solute concentration (mol/volume), and $\mathbf{f}_{\text{mem}}$ is the membrane stress that consists of both bending $\mathbf{f}_{\text{ben}} = -k_b\mathbf{x}_{ssss}$ and tension $\mathbf{f}_{\text{ten}} = (\sigma\mathbf{x}_s)_s$, where s is the arclength, $\sigma = \Lambda - \frac{3}{2}\kappa^2$, Λ is the membrane tension, and κ is the membrane curvature.

Using $k_w \sim 10^{-12}$ $\text{m}^2\text{s/kg}$ and an osmolarity $\triangle c = 0.1$ mol/l (consistent with the osmotic filtration experiments [28]), the corresponding water flow is of the order $v_o = 0.1$ μm/s. Assuming a membrane bending stiffness of $k_b = 10^{-19}$ J, a membrane tension of 10^{-3} N/m (one tenth of the lysis tension), and a characteristic length scale of 10^{-6} m, the tension contribution (v_t) and elastic stress contribution (v_e) to the permeable water flow can be scaled to v_o as $v_o : v_t : v_e = 10^0 : 10^{-2} : 10^{-6}$. Furthermore, we note that in the absence of an osmotic stress ($\triangle c = 0$), the permeating water flow may be non-negligible when the membrane tension becomes large due to the external stress such as the hydrodynamic stress from an external flow or confinement. In this work we set $\triangle c = 0$ in Eq. (1) to focus on the water flux driven by the pressure difference due to an external flow or confinement.

In our formulation, a semipermeable vesicle is suspended in a viscous Newtonian fluid (in domain Ω). The vesicle membrane γ is parameterized as $\mathbf{x}(s, t)$ where s is arclength and t is time. In the suspending fluid the flow velocity $\mathbf{u}$ and pressure p are governed by the incompressible Stokes equations

$$-\nabla p + \mu\triangle\mathbf{u} = 0, \quad \nabla \cdot \mathbf{u} = 0, \qquad \mathbf{x} \in \Omega \setminus \gamma, \tag{2}$$

where μ is the fluid viscosity. When Ω is an unconfined geometry, the condition $\mathbf{u}(\mathbf{x}) \to \mathbf{u}_\infty(\mathbf{x})$ as $|\mathbf{x}| \to \infty$ is enforced. Along the vesicle membrane γ, mass continuity, force balance, and local inextensibility are enforced by requiring

$$[\![\mathbf{u}]\!]_\gamma = 0, \quad [\![\mathbf{T} \cdot \mathbf{n}]\!]_\gamma = \mathbf{f}_{\text{mem}}, \quad \mathbf{x}_s \cdot \mathbf{u}_s = 0, \tag{3}$$

where $[\![\cdot]\!]_\gamma$ is the jump across the interface and $\mathbf{T} = -p\mathbf{I} + \mu(\nabla\mathbf{u} + \nabla\mathbf{u}^T)$ is the hydrodynamic stress tensor.

We nondimensionalize the governing equations [Eqs. (1)–(3)] by a characteristic length scale $R_0 = 10^{-6}$ m, a bending stiffness $k_b = 10^{-19}$ J, and fluid viscosity 5×10^{-2} kg/ms. We scale time by $\tau = \mu R_0^3/k_b = 0.5$ s, the velocity by $R_0/\tau = 2$ μm/s, the pressure by $k_b/R_0^3 = 10^{-1}$ Pa, the tension by $k_b/R_0^2 = 10^{-7}$ N/m, and the permeability by $R_0/\mu = 10^{-3}\text{m}^2\text{s/kg}$. Under this nondimensionalization suitable for a vesicle in a quiescent flow, a two-dimensional semipermeable vesicle in a viscous fluid is characterized by (a) its reduced area $\alpha = 4\pi A/L^2 \in (0, 1]$, where L is the vesicle length and A is its area, and (b) its permeability $\beta = k_w\mu/R_0$. In two dimensions, the conservation of total lipids in the membrane corresponds to the inextensibility (fixed length L) of γ. Due to semipermeability to water ($\beta > 0$), the enclosed area A is not conserved and the reduced area α is dynamic.

Since the fluid satisfies the Stokes equations, the velocity and pressure can be represented as layer potentials. Given the interfacial boundary conditions in Eq. (3), the fluid velocity is

$$\mathbf{u}(\mathbf{x}) = \mathbf{u}_\infty(\mathbf{x}) + \mathcal{S}[\mathbf{f}_{\text{mem}}](\mathbf{x}), \quad \mathbf{x} \in \Omega, \tag{4}$$

where $\mathcal{S}$ is the single-layer potential

$$\mathcal{S}[\mathbf{f}](\mathbf{x}) = \frac{1}{4\pi}\int_\gamma \left(-\mathbf{I}\log\rho + \frac{\mathbf{r}\otimes\mathbf{r}}{\rho^2}\right)\mathbf{f}(\mathbf{y})ds_\mathbf{y}, \tag{5}$$

with $\mathbf{r} = \mathbf{x} - \mathbf{y}$ and $\rho = |\mathbf{r}|$. Together with the inextensibility constraint and the dimensionless boundary condition

$$\mathbf{u} - \dot{\mathbf{x}} = -\beta(\mathbf{f}_{\text{mem}} \cdot \mathbf{n})\mathbf{n}, \qquad \mathbf{x} \in \gamma, \tag{6}$$

the vesicle membrane velocity satisfies the boundary integral equation

$$\dot{\mathbf{x}} = \mathbf{u}_\infty(\mathbf{x}) + \beta(\mathbf{f}_{\text{mem}} \cdot \mathbf{n})\mathbf{n} + \mathcal{S}[\mathbf{f}_{\text{mem}}](\mathbf{x}), \quad \mathbf{x}_s \cdot \dot{\mathbf{x}}_s = 0. \tag{7}$$

In confined geometries, the far-field term $\mathbf{u}_\infty(\mathbf{x})$ is replaced by a double-layer potential with an unknown density defined on $\partial\Omega$. The density function is used to satisfy the boundary condition on $\partial\Omega$. Specifically, in the two examples of a semipermeable vesicle under strong confinement, we enforce a no-slip boundary condition along the top and bottom of the channel and a Hagen-Poiseuille flow at the inlet and outlet—this boundary condition has been used in similar vesicle setups [35–37].

The value of β can be estimated by first converting the apparent permeability of a membrane [28] to the hydraulic conductivity k_w using the conversion in Fettiplace and Haydonn [22] and then scaling k_w to R_0/μ. We found that for most lipid bilayer membranes, $10^{-14} \leqslant k_w \leqslant 10^{-12}$ m^{2}s/kg, thus the range of β corresponding to the native water permeability of a lipid bilayer membrane (vesicle) is $10^{-11} \leqslant \beta \leqslant 10^{-9}$, consistent with the value in Vogl *et al.* [33]. The cellular nuclear envelop is often treated as a filtration membrane [38], and its hydraulic conductivity is reported to be orders of magnitude larger [39]: $10^{-11} \leqslant k_w \leqslant 10^{-9}$ m^{2}s/kg, and the corresponding range of β (using the same R_0/μ for scaling) is $10^{-8} \leqslant \beta \leqslant 10^{-6}$.

For the simulations in Sec. IV and Sec. V we use a wider range of β to elucidate the effects of permeating water flow across a semipermeable inextensible membrane. For example, we use $10^{-5} \leqslant \beta \leqslant 10^{-2}$ in our simulations of a semipermeable inextensible membrane in free space under various flowing conditions. We found that the equilibrium shape of a semipermeable membrane in free space to be independent of β. Within this range of β we find that β only affects the time it takes for the membrane to reach the equilibrium shape, which is determined by the background flow (such as a quiescent flow, a linear shear flow and its shear rate, and a Poiseuille flow and its maximum velocity). From these results and our analysis of areal dynamics, we suspect similar hydrodynamics of a semipermeable vesicle (with $10^{-11} \leqslant \beta \leqslant 10^{-9}$). When we use $\beta \geqslant 0.1$, we find that the semipermeable membrane swells to maximize its water content, independent of the initial reduced area and the background flow.

On the other hand, under strong confinement, we find that $10^{-4} \leqslant \beta \leqslant 10^{-3}$ is needed in our simulations to keep the membrane tension below the threshold value $\sim 10^{-3}$ N/m for poration in a lipid bilayer membrane. Such range of β may imply that a vesicle would be porated under large stress caused by confinement.

A. Equilibrium and areal dynamics in a quiescent flow

In the absence of an imposed flow, the steady equilibrium shape and a differential equation for the area inside the semipermeable inextensible membrane can be derived by following the analysis of Veerapaneni *et al.* [40] in a quiescent flow ($\mathbf{u}_\infty = 0$). The steady-state shape is a fixed point of

the Lagrangian

$$\mathcal{L} = \frac{1}{2}\int_\gamma \kappa^2\, ds + \Lambda\left(\int_\gamma ds - L\right), \tag{8}$$

where the Lagrange multiplier Λ is the tension. Note the absence of the pressure Lagrange multiplier since the total water content inside the vesicle membrane is not conserved. Taking the variation of $\mathcal{L}$ with respect to γ and setting it to zero, the steady-state shape satisfies $\kappa_{ss} + \frac{1}{2}\kappa^3 - \Lambda\kappa = 0$, with initial conditions $\kappa(0) = \kappa_0$ and $\kappa_s(0) = 0$. Multiplying by κ_s and integrating once, we have

$$\frac{\kappa_s^2}{2} + \frac{\kappa^4}{8} - \frac{\Lambda}{2}\kappa^2 = \frac{\kappa_0^4}{8} - \frac{\Lambda}{2}\kappa_0^2. \tag{9}$$

Assuming $\kappa_s \neq 0$, Eq. (9) is separable, and can be solved analytically in terms of the *EllipticF* function using Mathematica. Unlike in the impermeable case, the solution of Eq. (9) is not periodic unless $\kappa(s) = \kappa_0$. Therefore, the equilibrium shape of a semipermeable vesicle in a quiescent flow is a circle with radius $L/2\pi$ and constant tension $\Lambda = \kappa^2/2 = 2\pi^2/L^2$. Note that in contrast to a impermeable vesicle, the steady-state tension is positive rather than negative. The equilibrium shape of a semipermeable vesicle results from the balance between elastic stress and membrane tension. For an elastic membrane with a large pore, the equilibrium membrane (hemispherical) shape also results from such a balance [41].

We next compute the areal dynamics of a semipermeable vesicle. Since the area of the vesicle is

$$A(t) = \frac{1}{2}\int_\gamma (\mathbf{x}\cdot\mathbf{n})\, ds, \tag{10}$$

its derivative includes terms due to the time derivative of $\mathbf{x}\cdot\mathbf{n}$ and a term due to interface stretching [42], but this latter term is zero because of the local inextensibility condition. Therefore,

$$\dot{A}(t) = \frac{1}{2}\int_\gamma (\dot{\mathbf{x}}\cdot\mathbf{n})\, ds + \frac{1}{2}\int_\gamma (\mathbf{x}\cdot\dot{\mathbf{n}})\, ds. \tag{11}$$

Applying integration by parts, the two integrals are identical and we combine them to obtain

$$\dot{A}(t) = \int_\gamma (\beta(\mathbf{f}\cdot\mathbf{n})\mathbf{n} + \mathcal{S}[\mathbf{f}])\cdot\mathbf{n}\, ds = \beta\int_\gamma (\mathbf{f}\cdot\mathbf{n})\, ds, \tag{12}$$

where we have used the incompressibility of the single-layer potential. Substituting in $\mathbf{f} = \mathbf{f}_{\text{ben}} + \mathbf{f}_{\text{ten}}$ and repeatedly applying integration by parts, we obtain

$$\dot{A}(t) = \beta\int_\gamma \left(\frac{\kappa^3}{2} - \kappa\Lambda\right) ds. \tag{13}$$

Note that the integrand in Eq. (13) is zero when the membrane tension balances the elastic force

$$\Lambda = \frac{\kappa^2}{2} = \frac{\kappa_0^2}{2}, \tag{14}$$

which is consistent with the equilibrium result in Eq. (9).

III. NUMERICAL METHODS

In the boundary integral equation formulation, the unknowns are the vesicle's position and tension. With confinement, an extra unknown (the density function) is added to enforce the no-slip boundary conditions on the confinement wall. Both γ and $\partial\Omega$ are discretized at a set of collocation points. Derivatives are computed with Fourier differentiation, and the weakly singular single-layer potential is computed with an eighth-order quadrature rule [43]. For confined geometries, the trapezoid rule is used to approximate the double-layer potential since its kernel is smooth and periodic. Nearly singular integrals are computed with an interpolation-based quadrature rule [35].

A. Discretization in time

We apply a second-order spectral deferred correction (SDC) method that was thoroughly tested in previous work [44]. To control error over long time horizons, we use the error in length to adaptively adjust the time step size. Our SDC formulation requires two applications of a first-order time-stepping method. To allow for large time step sizes, terms involving high-order derivatives are discretized semi-implicitly. We start by defining

$$\mathcal{B}\mathbf{f} = -\frac{d^4}{ds^4}\mathbf{f}, \qquad \mathcal{T}\sigma = (\sigma \mathbf{x}_s)_s, \quad \mathcal{D}\mathbf{f} = \mathbf{x}_s \cdot \mathbf{f}_s, \quad P\mathbf{f} = (\mathbf{f}\cdot\mathbf{n})\mathbf{n}, \tag{15}$$

for the differential and projection operators. Then Eq. (7) can be written as

$$\dot{\mathbf{x}} = \mathbf{u}_\infty(\mathbf{x}) + \beta P(\mathcal{B}\mathbf{x} + \mathcal{T}\sigma) + \mathcal{S}(\mathcal{B}\mathbf{x} + \mathcal{T}\sigma), \quad \mathcal{D}\dot{\mathbf{x}} = 0. \tag{16}$$

We note that the operators defined in Eq. (15) and the single-layer potential defined in Eq. (5) depend on the vesicle shape. A time-stepping method that treats these dependencies implicitly would result in a nonlinear set of equations that would be computationally expensive to solve. Instead, we define the operators at time t^N and discretize the stiff terms due to high-order derivatives implicitly [35,45]. In particular, the first-order semi-implicit method that is applied iteratively within SDC is

$$\frac{\mathbf{x}^{N+1} - \mathbf{x}^N}{\triangle t} = \mathbf{u}_\infty(\mathbf{x}^N) + \beta P^N\left(\mathcal{B}^N\mathbf{x}^{N+1} + \mathcal{T}^N\sigma^{N+1}\right) + \mathcal{S}^N\left(\mathcal{B}^N\mathbf{x}^{N+1} + \mathcal{T}^N\sigma^{N+1}\right), \tag{17}$$

$$\mathcal{D}^N\mathbf{x}^{N+1} = 1, \tag{18}$$

and this linear system is solved with matrix-free GMRES.

B. Numerical validation

To validate our numerical codes for simulating vesicle hydrodynamics, we reproduce a phase diagram of the equilibrium shape of an impermeable vesicle in a Poiseuille flow. Depending on the maximum flow velocity and the vesicle reduced area, the equilibrium vesicle shape is either an axisymmetric bullet, an axisymmetric parachute, or a tank-treading asymmetric slipper [46]. Comparing against the simulation results of an impermeable vesicle in Poiseuille flow (specifically Fig. 2 in Kaoui *et al.* [46]), we observe general agreement in the equilibrium vesicle shapes, see Fig. 2.

IV. HYDRODYNAMICS OF A SEMIPERMEABLE INEXTENSIBLE MEMBRANE IN FREE SPACE

To highlight the effects of membrane permeability to water, we consider a single semipermeable inextensible membrane, with (dimensionless) permeability coefficient $\beta > 0$, in familiar configurations: In free space we place a semipermeable inextensible membrane in a quiescent flow, a planar shear flow, and a Poiseuille flow. For each example, we fix the membrane length and examine the enclosed water content as a dynamic consequence of water flow, membrane shape deformation, and distribution of membrane tension. Under these flows, our simulations show that the steady state of an impermeable vesicle is different from that of a semipermeable inextensible membrane, which depends only on the strength of the external flow and is insensitive to permeability β (as long as $\beta > 0$). We find that the time in the dynamic evolution toward equilibrium is scaled by β^{-1}: The smaller β is the longer it takes to reach the steady state.

In experiments, vesicles under shear flows are measured for a few minutes (chapter 19 in Ugarte-Uribe *et al.* [26]), a duration over which a vesicle can be assumed impermeable [47]. Our simulations of a semipermeable vesicle under these flows in open geometry show that water permeability may lead to different membrane hydrodynamics only after a duration of $\sim$1 day.

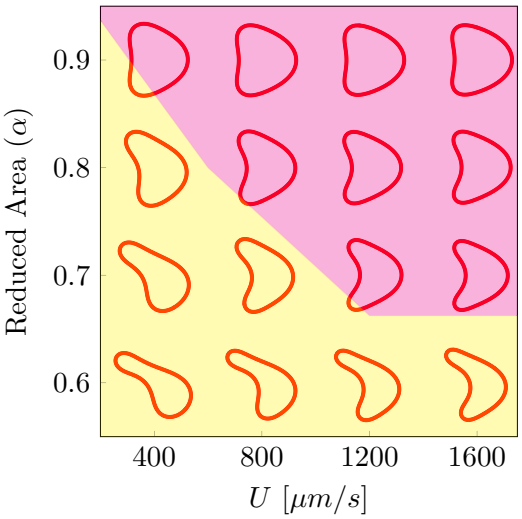

FIG. 2. Phase diagram of an impermeable vesicle with various reduced areas submerged in a Poiseuille flow with various flow rates. The shapes agree with Kaoui *et al.* [46] (see Fig. 2).

A. Quiescent flow

In the absence of a background flow, a semipermeable inextensible membrane in free space is quantified in terms of its areal dynamics and transition to the equilibrium shape, which is a circular membrane with a uniform membrane tension $\Lambda = 2\pi^2/L^2$. This is in stark contrast with the impermeable vesicle relaxing to equilibrium that depends on the vesicle reduced area, which remains constant for $\beta = 0$. Our analysis in Sec. II A shows that a semipermeable inextensible membrane relaxes to a circle at a rate that is proportional to β, regardless of the initial membrane shape (for a fixed length). For this reason, our numerical results are reported in terms of the scaled time βt.

In Fig. 3, we examine the relaxation dynamics with four initial shapes and reduced areas as labeled. The membrane shapes on the left are color coded by the water permeation flux: Red denotes an influx into the membrane, and blue denotes an efflux out of the membrane. First we observe that the initial membrane shape determines the direction of water flux. For the case with an initial reduced area $\alpha(0) = 0.12$ (bottom row) the membrane deflates (blue regions) first due to the high interior capillary pressure that corresponds to the high membrane curvatures. For the other three cases efflux is dominated by influx, especially after $t = 1$ day when the increase in total water content becomes non-negligible. Over time (about 4 weeks) all cases inflate and as expected, each case eventually reaches a circular shape with reduced area $\alpha = 1$.

Between $t = 30$ minutes and $t = 1$ day, the total water content is nearly constant. This can be explained by considering the two terms that contribute to the vesicle velocity: (i) the permeability velocity, $\beta(\mathbf{f} \cdot \mathbf{n})\mathbf{n}$, and (ii) the force balance velocity, $\mathcal{S}[\mathbf{f}]$. Since $\beta \ll 1$, the permeability velocity is much smaller than the force balance velocity at early times, and the dynamics of a semipermeable inextensible membrane resemble those of an impermeable vesicle. As the force balance velocity decreases, the permeability velocity dominates, and the vesicle begins to inflate to a circle with vanishing force and velocity.

Figure 4 shows the tension distribution along the relaxing membranes in Fig. 3. The membrane tension (color bars) is in N/m. As the semipermeable inextensible membrane relaxes, the membrane tension reduces in magnitude and becomes more evenly distributed along the membrane. In the top row [$\alpha(0) = 0.95$] the membrane nearly relaxes to a circle on the right, and the membrane tension is uniform and equal to $k_b\kappa_0^2/2$ as predicted by our analysis in Eq. (14).

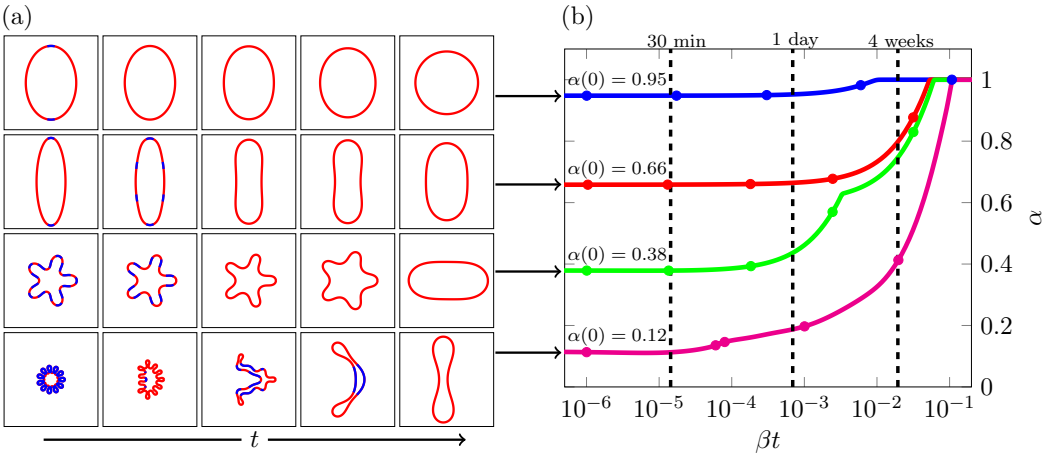

FIG. 3. (a) Snapshots of four semipermeable inextensible membranes with $\beta = 10^{-8}$ submerged in a fluid with no background flow. Time goes from left to right. The red regions correspond to influx and the blue regions correspond to efflux. In all cases, the vesicle reaches a steady-state circular shape. (b) The reduced area of each of the simulations. The particular snapshots in (a) occur at the marks along the curve. Three dimensioned times are denoted by the dashed lines.

B. Planar shear flow

We consider a semipermeable inextensible membrane in a planar shear flow, characterized by the elastic capillary number $\mathrm{Ca}_E = \chi\tau$ where τ is the characteristic timescale from balancing the viscous stress with the elastic stress (see Sec. II) and χ is the shear rate of the planar shear flow $\mathbf{u}_\infty(\mathbf{x}) = \chi(y, 0)$. When $\beta = 0$ (impermeable case), the vesicle reduced area and fluid viscosity

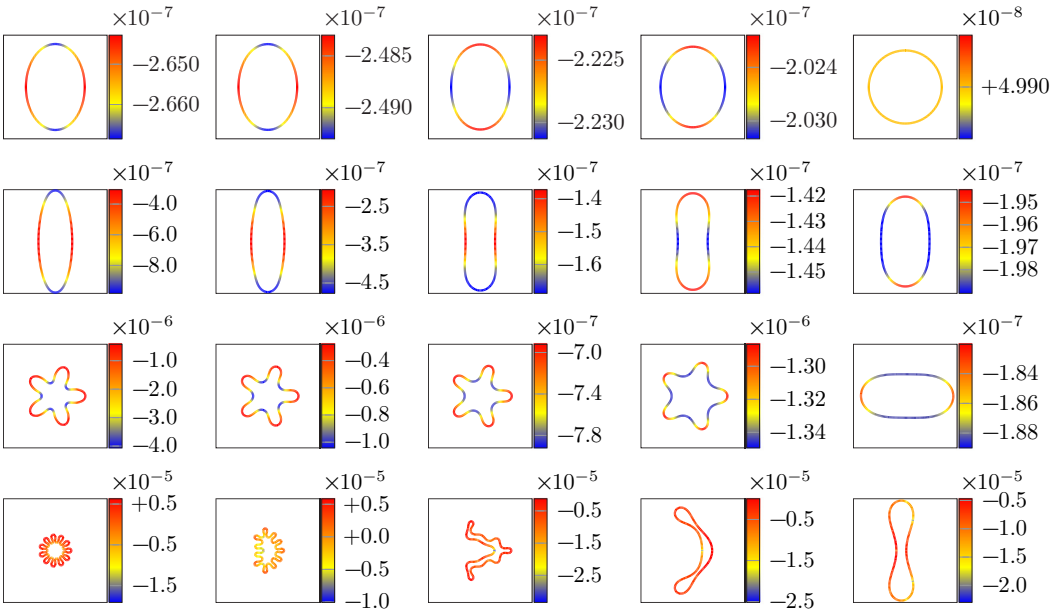

FIG. 4. The distribution of membrane tension corresponding to the relaxation dynamics in Fig. 3.

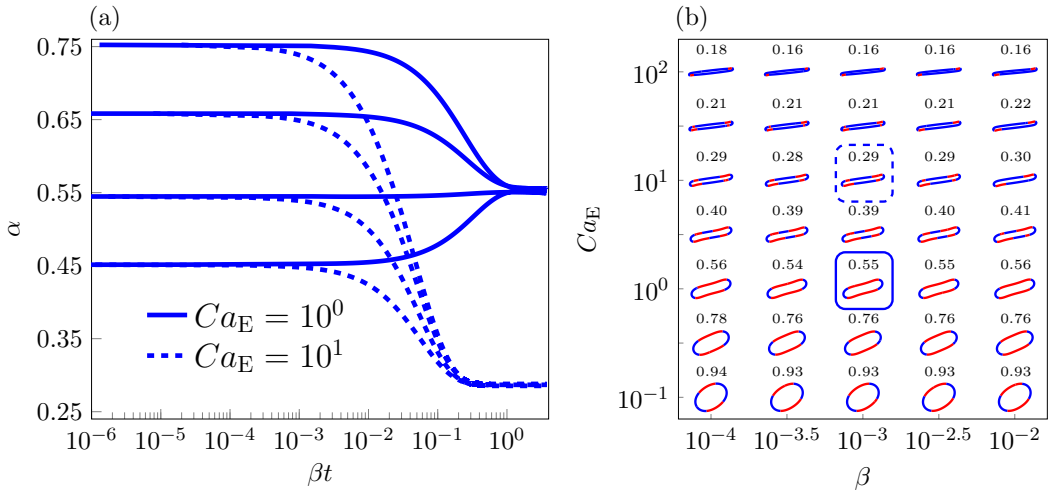

FIG. 5. (a) The reduced area of a semipermeable inextensible membrane with $\beta = 10^{-3}$ initialized with four different reduced areas in a shear flow with two different flow rates. (b) The equilibrium membrane shape with varying flow rates and membrane permeability. The red regions correspond to influx and the blue regions correspond to efflux. The boxed membranes correspond to the simulation results in part (a).

contrast determine whether a vesicle tank treads or tumbles [48,49]. Focusing on a semipermeable inextensible membrane with no viscosity contrast, we find that the membrane tilts to an inclination angle and undergoes tank-treading dynamics, similar to the case of an impermeable vesicle.

In Fig. 5(a), using four initial reduced areas and two flow rates, we plot the reduced area of a semipermeable inextensible membrane with $\beta = 10^{-3}$. As observed in a quiescent flow, the final membrane shape is independent of the initial reduced area. However, it does depend on the flow rate. We also observe that the amount of water inside the vesicle remains constant until $t \sim 2$ h, when the normal component of the flow velocity becomes significantly smaller than the permeable velocity, leading to a changing reduced area.

For a range of dimensionless permeability coefficient $\beta > 0$ and capillary number Ca_E, a semipermeable inextensible membrane reaches an equilibrium shape as in Fig. 5(a). Since the equilibrium shape depends on Ca_E and is independent of the initial reduced area, we initialize the membrane with reduced area $\alpha = 0.65$ for all simulations in Fig. 5(b), where we summarize the equilibrium membrane shape and its reduced area. We see that the capillary number (flow rate) significantly affects the final membrane shape, but the permeability coefficient has a very minor effect on the equilibrium shape for $10^{-4} \leqslant \beta \leqslant 10^{-2}$. Instead, β sets the time required for a membrane to reach its steady-state configuration which is proportional to β^{-1}, as we saw in the analysis for the quiescent flow (Sec. II A).

The tension distribution along the equilibrium membrane shape at $\beta = 10^{-4}$ is shown in Fig. 6, where the color bars are the membrane tension in N/m. The capillary number Ca_E increases from Figs. 6(a)–6(d), and we observe that the tension magnitude also increases almost linearly with Ca_E. We also observe that the membrane tension is relatively small at the tip when the membrane curvature is large due to the extensional component in the shear flow.

C. Poiseuille flow

We consider a semipermeable inextensible membrane in the Poiseuille flow $\mathbf{u}_\infty(\mathbf{x}) = U(1 - (y/W)^2, 0)$, where U is the maximum velocity at $y = 0$. The nonlinear effects of the Poiseuille flow on the migration of an impermeable vesicle have been well studied [46]: At a given value of the maximum velocity U, there exists a critical reduced volume above which the equilibrium vesicle

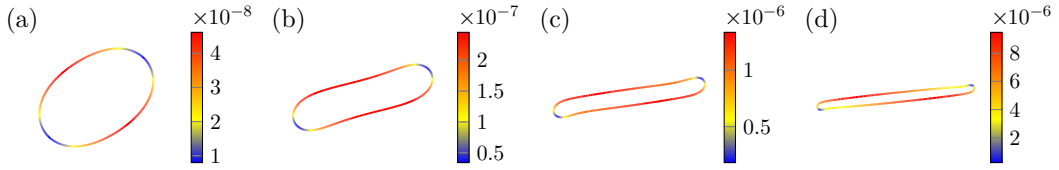

FIG. 6. The tension distribution along a semipermeable inextensible membrane in a linear shear flow. The semipermeability constant is $\beta = 10^{-4}$ for all these cases, and the elastic capillary numbers are (a) 10^{-1}, (b) 10^{0}, (c), 10^{1}, and (d) 10^{2} as in Fig. 5(b).

shape is symmetric (parachute or bullet shapes) and the vesicle stays at $y = 0$. Below this critical reduced volume the equilibrium vesicle moves off the center and is asymmetric (tank-treading slipper shape). We validated our numerical codes by comparing against results in Kaoui *et al.* [46] (see Sec. III B).

At the beginning of the simulations, a semipermeable vesicle is placed above the center line $y = 0$ and it migrates toward the center line as in the impermeable case [50]. Using several initial reduced areas and flow rates, we recreate the impermeable vesicle phase diagram for semipermeable vesicles with $\beta = 10^{-3}$. Smaller values of β have been used for some parameters but the time it takes to reach equilibrium (for some this involves a transient tank-treading motion along the membrane to gradually slow down in the presence of small β) is too long in these simulations.

The equilibrium membrane shape for different U and initial reduced area is summarized in Fig. 7(a), and the vertical displacement of the vesicle's center-of-mass is in Fig. 7(b). The effect of semipermeability of a vesicle with $\alpha(0) = 0.9$ and $U = 800$ μm/s on its reduced area and migration pattern are shown in Figs. 7(c) and 7(d), respectively.

As observed for the linear shear flow, our simulations show that the equilibrium reduced area of a semipermeable inextensible membrane in a Poiseuille flow is independent of the initial reduced area. Instead we find that larger maximum flow velocity U results in smaller equilibrium reduced area [Fig. 7(a)]. At the smallest velocity $U = 200$ μm/s, the steady-state reduced area is large, and the equilibrium vesicle shape is an axisymmetric bullet. The equilibrium reduced area decreases with increasing U, and the nonlinear flow profile gives rise to an asymmetric tank-treading slipper for $U \geqslant 400$ μm/s. We observe that the membrane permeability to water drastically alters the equilibrium vesicle shape and position relative to the Poiseuille flow: At $\beta = 10^{-3}$ the equilibrium vesicle depends only on the maximum velocity U of the nonlinear shear flow. The higher U the smaller the equilibrium reduced area and the farther away the vesicle is relative to the flow center at $y = 0$.

The membrane tension distribution of the equilibrium shapes are shown in Fig. 8 for the flow velocities U from 200 to 800 μm/s. We note that in the Poiseuille flow the membrane tension is positive in the front, and negative in the rear part of the vesicle. Furthermore we also note that the tension magnitude is almost linearly proportional to U as in the linear shear flow.

D. Contribution from membrane tension and bending to the permeating flux

In the absence of viscosity contrast between interior and exterior fluids, the pressure jump is $[\![p]\!]_\gamma = \mathbf{f}_{\text{mem}} \cdot \mathbf{n}$ [51]. Thus in our model, the permeating flux is proportional to the normal component of membrane forces $\mathbf{f}_{\text{mem}} \cdot \mathbf{n}$. We decompose $\mathbf{f}_{\text{mem}} \cdot \mathbf{n}$ into its contributions due to tension and bending as

$$\mathbf{f}_{\text{ten}} \cdot \mathbf{n} = -\kappa \Lambda \quad \text{and} \quad \mathbf{f}_{\text{ben}} \cdot \mathbf{n} = \kappa_{ss} + \tfrac{1}{2}\kappa^3. \tag{19}$$

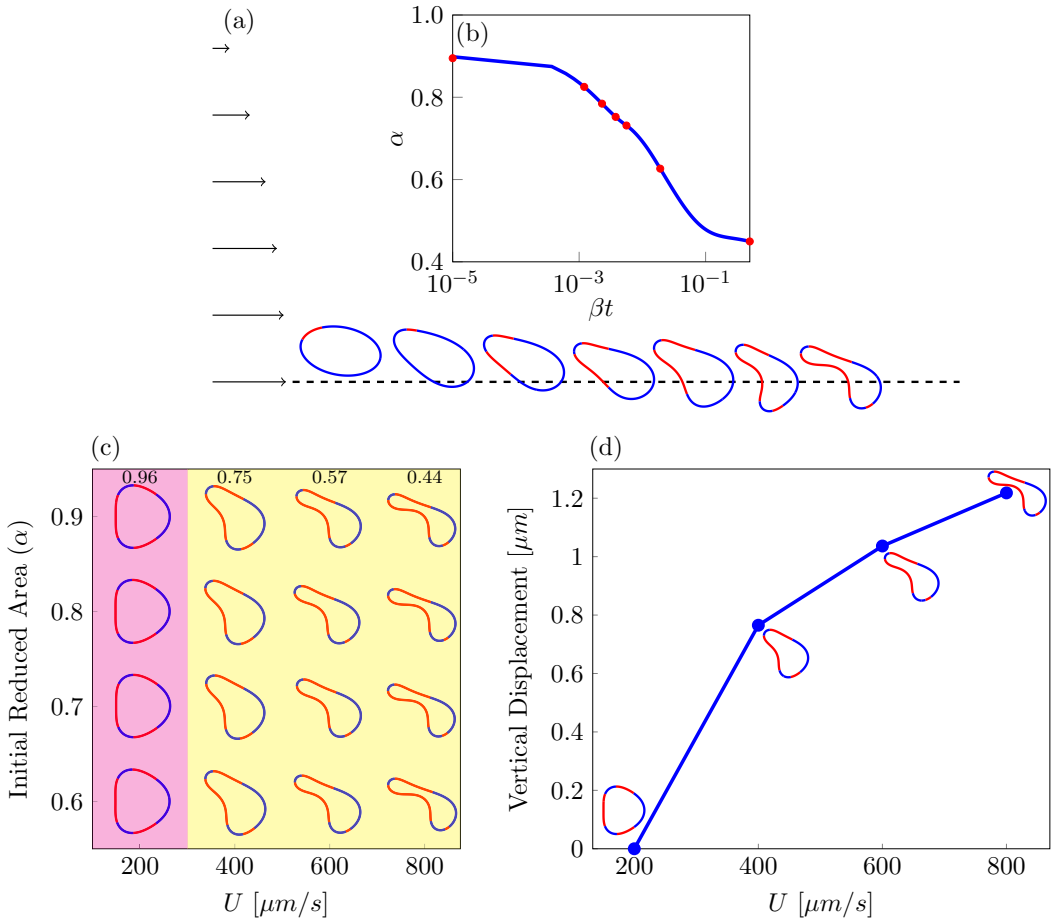

FIG. 7. (a) A semipermeable membrane suspended in a Poiseuille flow with maximum velocity 800 μm/s. The channel width is 12.5 times larger than the vesicle radius. (b) The reduced area of the vesicle as a function of time. The red marks correspond to the vesicle shapes in (a). (c) The equilibrium shape of a semipermeable inextensible membrane submerged in a Poiseuille flow with varying initial reduced areas and flow rates. The red regions correspond to influx and the blue regions correspond to efflux. (d) The steady-state vertical displacement at four different flow velocities.

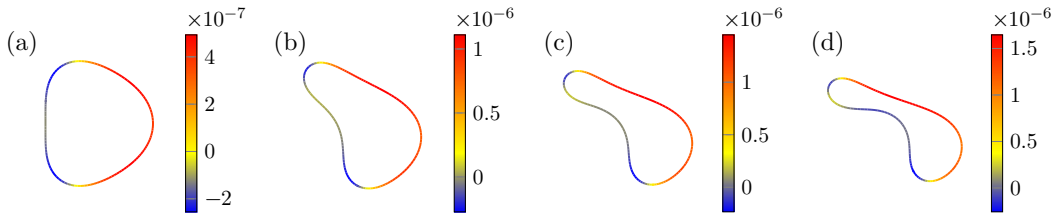

FIG. 8. The equilibrium tension distribution of a semipermeable inextensible membrane with $\beta = 10^{-3}$ in a parabolic flow (Fig. 7). The maximum flow velocities are (a) 200 μm/s, (b) 400 μm/s, (c) 600 μm/s, and (d) 800 μm/s.

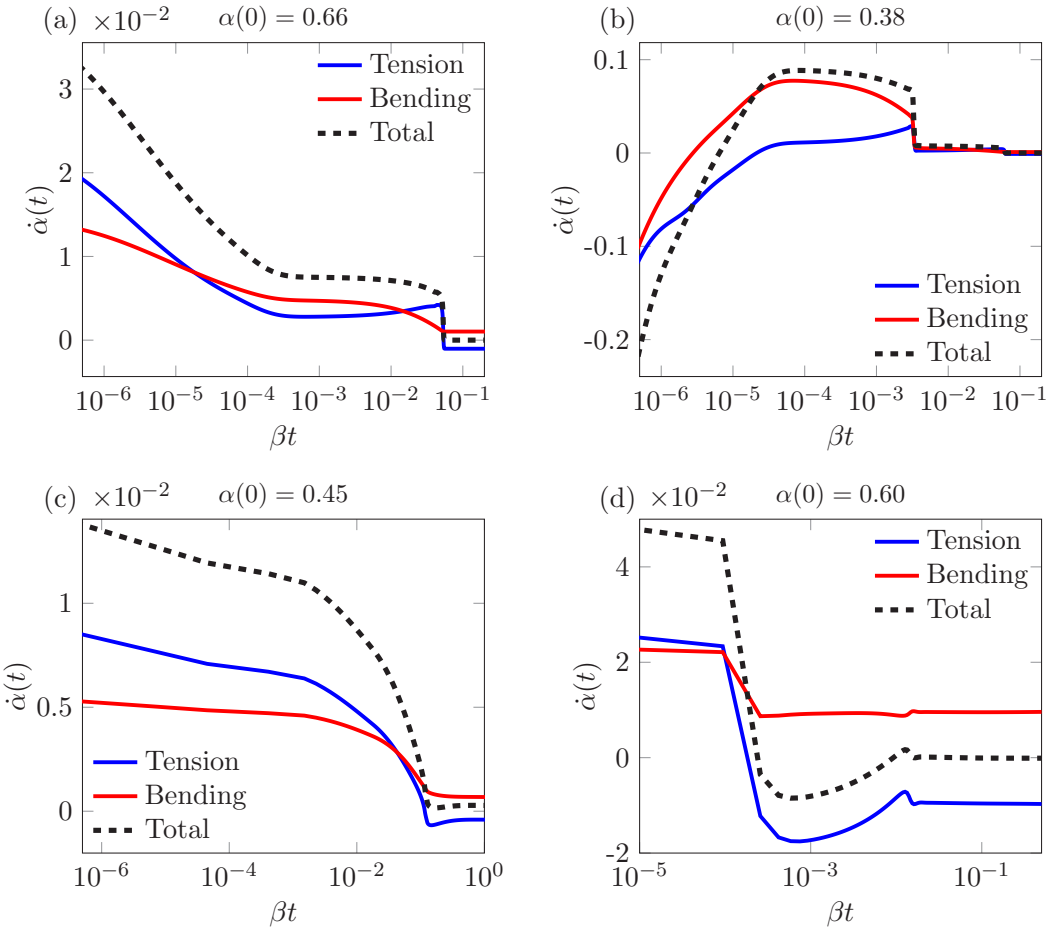

FIG. 9. The rate of change of the reduced area decomposed into contributions from membrane tension (blue curves) and membrane bending (red curves). The dashed line is the sum of these two contributions. (a) The quiescent example in Fig. 3 with $\alpha(0) = 0.66$. (b) The quiescent example in Fig. 3 with $\alpha(0) = 0.38$. (c) The planar shear example in Fig. 5 with $\alpha(0) = 0.45$ and $\mathrm{Ca}_E = 10^0$. (d) The Poiseuille example in Fig. 7 with $\alpha(0) = 0.60$ and maximum velocity $U = 600\ \mu$m/s.

Then, the total flux through the membrane due to the tension and bending forces are

$$\dot{A}_{\text{ten}}(t) = -\beta \int_\gamma \kappa \Lambda \, ds \quad \text{and} \quad \dot{A}_{\text{ben}}(t) = \frac{\beta}{2} \int_\gamma \kappa^3 \, ds, \tag{20}$$

respectively. Note that the sum of $\dot{A}_{\text{ten}}(t)$ and $\dot{A}_{\text{ben}}(t)$ results in Eq. (13). Multiplying (20) by $4\pi/L^2$, where L is the constant vesicle length, we obtain the rate of change of the reduced area due to the tension and bending forces. Figures 9 summarize the effect of the tension and bending forces on the semipermeability for two quiescent examples [Figs. 9(a) and 9(b)], one planar shear example [Fig. 9(c)], and one Poiseuille example [Fig. 9(d)]. In the quiescent flow examples, we see that the tension and bending forces result in similar amounts of semipermeability, and for the geometry with a larger initial curvature, the reduced area changes much quicker and the vesicle deflates at early times before inflating to a circular shape. In the planar shear flow and Poiseuille flow examples, the tension and bending forces result in similar amounts of semipermeability.

V. HYDRODYNAMICS OF A SEMIPERMEABLE INEXTENSIBLE MEMBRANE UNDER STRONG CONFINEMENT

Here we consider a semipermeable inextensible membrane under strong confinement: a long closely fit channel and a contracting channel. In a narrow microfluidic channel, a large pressure jump is often used to push the vesicle through a closely fit channel [52]. Our simulations show that such a configuration can lead to an amplification of water permeation at a fast timescale of the order of milliseconds. In addition, we find that a large value of β is needed to keep the membrane tension below the threshold value for membrane poration. Such high permeability for water may be regarded as an indication that the lipid bilayer membrane is porated under strong confinement, and our inextensible membrane model is for a porated vesicle within the Helfrich free energy framework. As in the previous examples, we fix the membrane length and examine the enclosed water content as a dynamic consequence of water flow, membrane shape deformation, and membrane tension distribution.

A. A semipermeable inextensible membrane in a closely fit channel (stenosis)

When red blood cells go through small capillary vessels, they experience large shape deformation and significant membrane stretching that triggers ATP release [14,15]. Many cells exhibit extraordinary flexibility as they go through narrow vessels [53], and adjustment of surface-to-volume ratio may be a key factor for a successful passage. Here we quantify the effect of water permeability on a vesicle going through a stenosis (a long microfluidic channel with a width smaller than the cell radius). Based on previous findings [52], we first examine the effect of semipermeability on the pressure fluctuation across a stenosed geometry. In this experiment, a pressure drop is used to squeeze a red blood cell through a constriction with diameter 5 μm and length 45 μm. We set up a similar computational geometry with a Poiseuille flow imposed at the inlet and outlet [Fig. 10(a)]. We set the maximum flow velocity to $U_{\max} = 1000$ μm/s at the inlet and outlet so that the residency time of the membrane in the stenosis channel is $t_R \approx 25$ ms which agrees with the experimental results [52]. When the red blood cell enters the channel, an increase in the pressure drop is required to maintain a constant flow rate, and the difference in the pressure drop is called the excess pressure.

We consider both an impermeable vesicle and semipermeable inextensible membrane with initial reduced area $\alpha = 0.65$ passing through a long narrow channel and compute the excess pressure as a function of vesicle position in the channel [Fig. 10(e)]. The impermeable case agrees with experimental results [52] (see Fig. 3). Our simulations show that less excess pressure is needed to drive a semipermeable inextensible membrane through the closely fit channel. Once in the channel, the vesicle takes a bullet shape with maximum tension in the front and minimum tension in the back [Fig. 10(c)], consistent with earlier results [19,54].

Figures 10(f) and 10(g) show that the semipermeable inextensible membrane deflates from the beginning due to the high flow velocity, consistent with the results for a vesicle in a Poiseuille flow in open space. As the membrane enters the stenosis channel, it continues to deflate in the front even though we observe influx (red segment) at various rear locations in the membrane. Overall, the membrane loses about 6.1% of its initial total water at a constant rate as shown in Figs. 10(f) and 10(g) (blue curves). Thus we expect that a larger amount of deflation is possible if the inextensible membrane is inside a longer stenosis: we consider a vesicle passing through a channel of triple the length in Fig. 10(b) and 10(d) with $U_{\max} = 1000$ μm/s, and we observe that vesicle stays inside the stenosis for a residence time $t_R \approx 70$ ms and the area decreases by 13.2% (red curves).

Figure 11 show the rate of change of the reduced area due to the tension force (blue), the bending force (red), and the total membrane force (black). In both short and long closely fit channels, the membrane tension is responsible for nearly all the permeating water flux. This is in contrast to the unconfined examples where the tension and bending forces were each responsible for a comparable amount of permeating water flux.

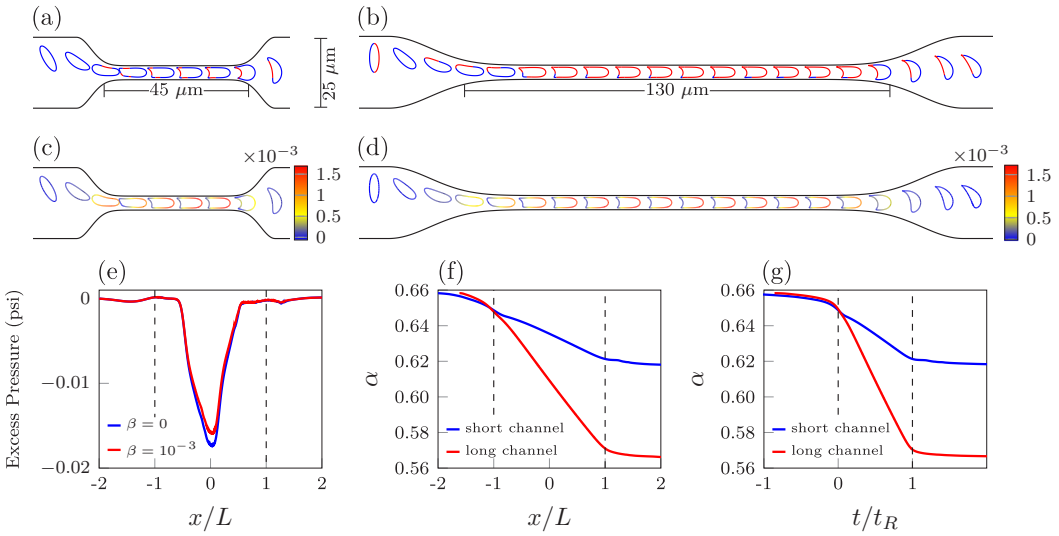

FIG. 10. (a) A semipermeable inextensible membrane passing through a closely fit channel similar to the experimental device in Abkarian *et al.* [52]. (b) A semipermeable inextensible membrane passing through a (three-times) longer closely fit channel than (a). In (a) and (b), red regions correspond to influx and blue regions correspond to efflux. [(c) and (d)] The tension in N/m of the vesicle shapes in (a) and (b). (e) The excess pressure of an impermeable and semipermeable inextensible membrane in the short geometry in (a). (f) The reduced area in the geometries in (a) and (b) as a function of the membranes' center-of-mass. In (e) and (f), the x axis is scaled by $1/L$ where L is half the length of the constriction. (g) The reduced area in the geometries in (a) and (b) as a function of time. The time axis is scaled by $1/t_R$ where t_R is the residency time. In (e) and (f), the dashed lines correspond to the locations of the inlet and outlet. In (g), the dashed lines correspond to the times that the vesicle enters and exits the constriction.

B. A semipermeable inextensible membrane in a contracting geometry

Squeezing a cell or a vesicle through a slit in microfluidics has gained popularity for its application in stress-induced release of macromolecules [17,54,56,57]. Red blood cells go through submicron slits many times during their lifetime, and this process selects healthy, flexible red blood cells to survive [55,58]. Here we investigate the role of membrane permeability to water when a semipermeable inextensible membrane is squeezed through a contracting microfluidic channel similar to Wu *et al.* [55], where the width of the channel gradually decreases from 18 to 1.8 μm. The channel then immediately reopens to 18 μm (Fig. 12). A Poiseuille flow is imposed at the inlet and outlet with a constant maximum flow rate of $U_{\max}$. We initialize a semipermeable inextensible membrane with $\alpha = 0.65$ that spans 10 μm of the total channel width and investigate the effects of the membrane permeability to water and the maximum flow velocity on whether a membrane can successfully pass through the slit.

In Figs. 12(a) and 12(b), we plot snapshots of membranes with different permeability β. Figure 12(c) shows the corresponding reduced area as a function of the membrane's location. We observe that if the permeability is sufficiently large, the vesicle inflates gradually over seconds before it reaches the neck, and then it quickly deflates within a fraction of a second. However, if the permeability β is too low, the membrane is too large when it reaches the narrowest part of the channel, and it is unable to pass. In Figs. 12(d) and 12(e), we plot snapshots of membranes with different imposed maximum velocities, and Fig. 12(f) shows the reduced area as a function of the membrane's location. At low velocities, the membrane inflates similar to the unbounded parabolic flow example, and it is unable to pass through the contraction. However, higher flow rates result in additional deflation and the membrane passes through the contraction. When the membrane is

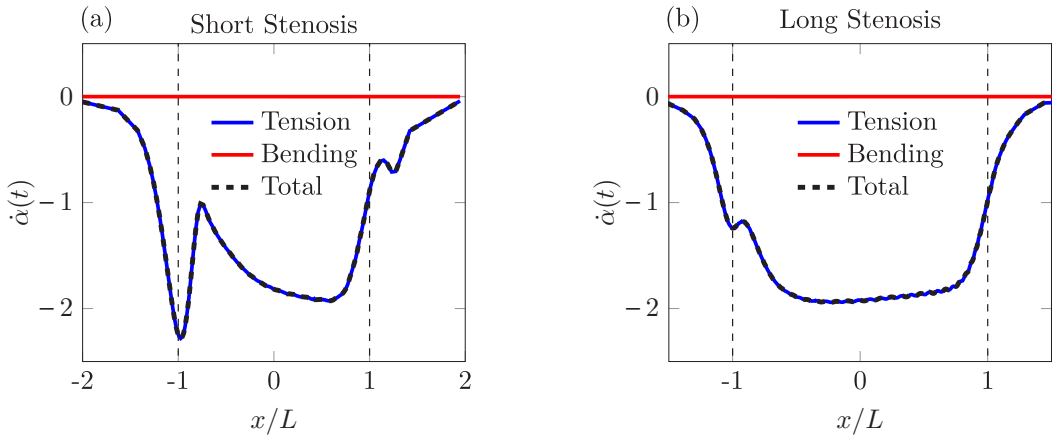

FIG. 11. The rate of change of the reduced area due to the membrane tension (blue curves) and membrane bending (red curves). The dashed line is the sum of these two contributions. (a) The short stenosis geometry in Fig. 10(a). (b) The long stenosis geometry in Fig. 10(b).

near the neck, simulations show that the water efflux is in the front and rear of membrane while most water influx is in the middle. The tension distribution along the membrane as a function of their position in the contracting channel is summarized in Figs. 12(g)–12(l), where we observe the tension has the largest magnitude when the membrane is at the neck.

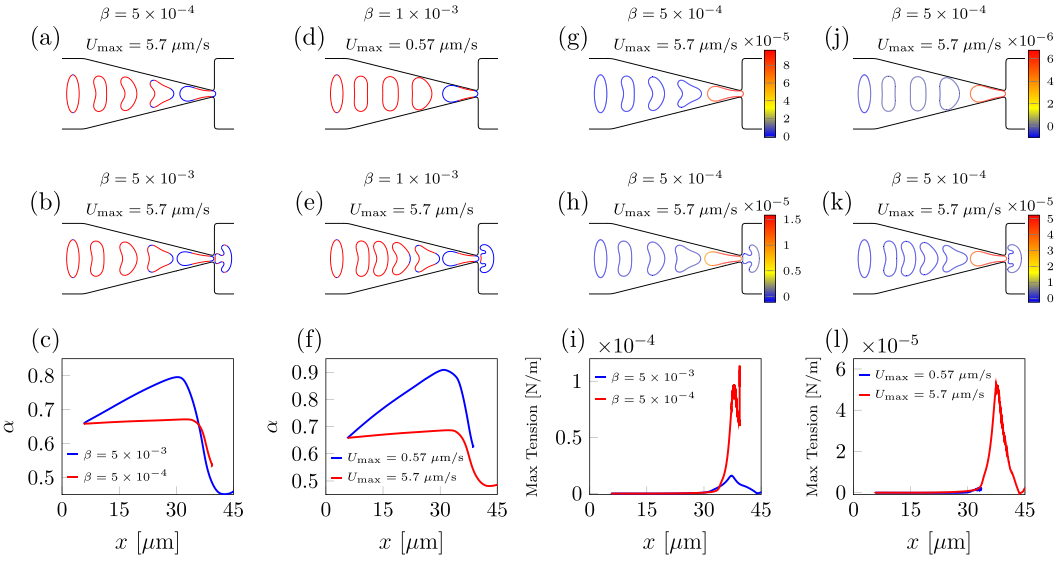

FIG. 12. A contracting channel similar to the experimental configuration in Wu *et al.* [55]. The channel width varies from 18 to 1.8 μm, and it repeats every 45 μm. The red regions correspond to influx and blue regions correspond to efflux [(a)–(c)] The ability for a semipermeable vesicle to pass through the contraction depends on the permeability β. [(d)–(f)] The ability for a semipermeable inextensible membrane to pass through the contraction depends on the flow rate. [(g)–(i)] The tension distribution and maximum tension in N/m of the vesicle shapes in (a) and (b). [(j)–(l)] The tension distribution and maximum tension in N/m of the vesicle shapes in (d) and (e).

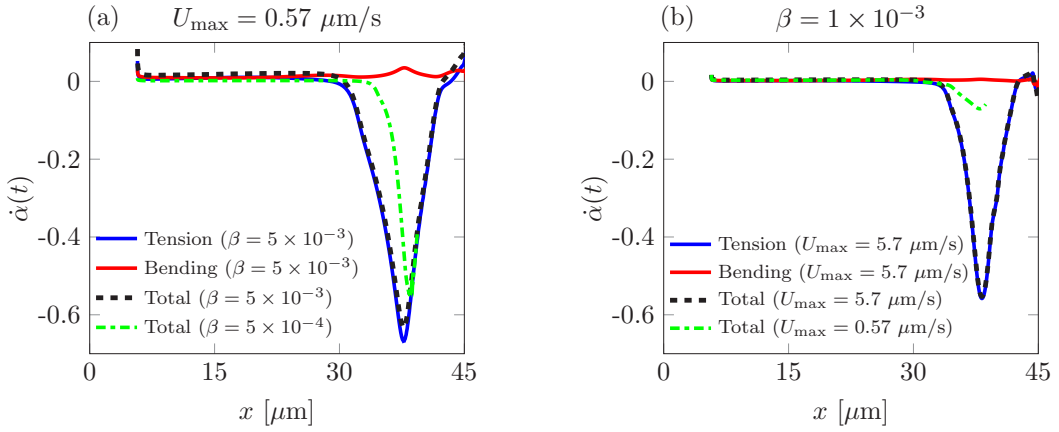

FIG. 13. The rate of change of the reduced area due to membrane tension (blue curves) and membrane bending (red curves). The dashed black line is the sum of these two contributions. Only simulations where the vesicle passes through the contraction are decomposed into the contributions due to tension and bending. (a) The low semipermeability coefficient in Fig. 12(b). The dash-dotted green curve corresponds to the simulation in Fig. 12(a). (b) The high semipermeability coefficient in Fig. 12(e). The dash-dotted green curve corresponds to the simulation in Fig. 12(d).

Figure 13 shows the rate of change of the reduced area due to membrane tension (blue curves), membrane bending (red curves), and the total membrane force (dashed black curves). Again, the tension is responsible for the majority of the permeating flux. While we only decompose the membrane force into tension and bending for the two vesicles that successfully pass through the contraction, we also plot the total membrane force for the two vesicles that do not pass through the contraction (dash-dotted green curves). The vesicle does deflate with a smaller semipermeability coefficient and a smaller maximum imposed velocity, but the rate of efflux is insufficient for successful passage of the vesicle through the contraction.

To understand the effects of water permeability on a semipermeable inextensible membrane that repeatedly passes through microcapillary vessels or submicron slits, we construct a contracting geometry (Fig. 14) to simulate a membrane passing through the contracting geometry six times. In Fig. 14(b), we show that the membrane deflates each time it passes through the contraction followed by a gradual inflation (over seconds). The total area loss over the history of the vesicle is almost 50%. In Fig. 14(c), we show the membrane center-of-mass velocity as a function of the membrane position. As the membrane passes through the contraction, it first accelerates until it reaches the neck where it abruptly decelerates to go through the contraction. Figure 14(d) shows the tension distribution, and the maximum tension is in Fig. 14(e). We see that the membrane tension is largest when it passes through the neck, and it is particularly large when it passes through the first neck since this is when the membrane has the largest area.

VI. DISCUSSION

In this work we investigate the effects of membrane permeability to water on the membrane hydrodynamics. Without any external flow or confinement, our analysis shows that a semipermeable inextensible membrane always inflates to maximize the water content inside the inextensible membrane [a fixed length (area) in two (three) dimensions]. Results from analysis and numerical simulations show that such relaxation of a semipermeable inextensible membrane is characterized by a rescaled time βt. In linear and nonlinear shear flows, we show that the steady-state shape depends on flow rate, while the permeability sets the timescale required to reach steady state. We further illustrate that the hydrodynamics consists of at least two phases. The first phase is dominated

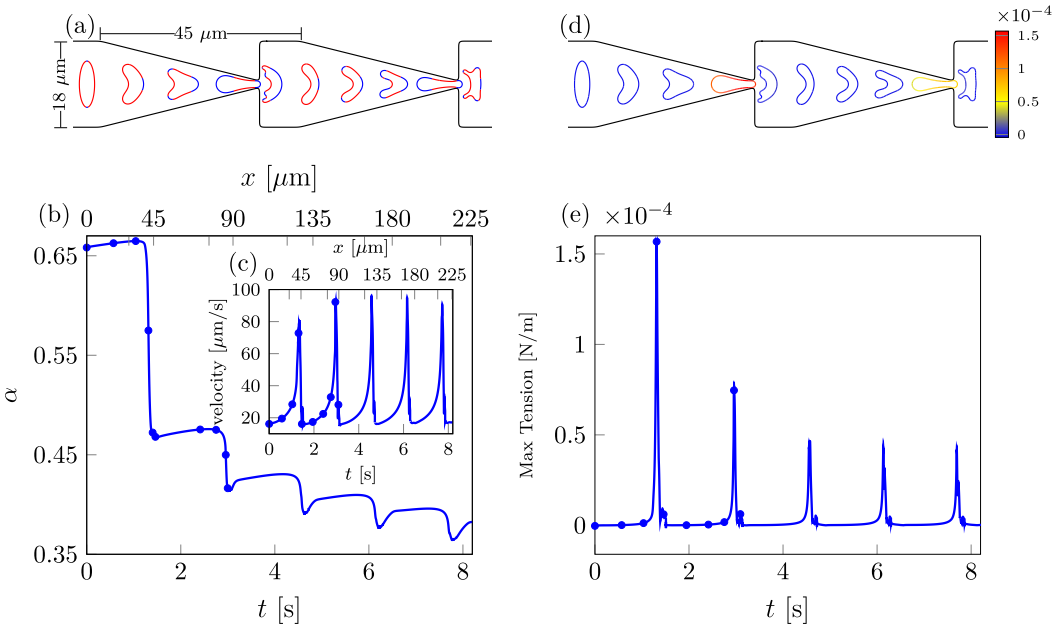

FIG. 14. The reduced area and velocity of a semipermeable inextensible membrane vs. time. The permeability coefficient is $\beta = 10^{-3}$ and the maximum velocity is 18 μm/s. (a) A semipermeable inextensible membrane passing through six periods of the contracting geometry. (b) The reduced area with the marks representing shapes in (a). (c) The center-of-mass velocity with the marks representing shapes in (a). In (b) and (c), the lower x axis is the x coordinate of the center-of-mass, and the upper x axis is time. (d) The membrane tension in N/m. (e) The maximum membrane tension.

by the balance between membrane traction and viscous stress at early times (up to 5 minutes), when the inextensible membrane behaves like an impermeable membrane. The second phase sets in after a few hours, when water flux begins to dominate and the semipermeable membrane either inflates or deflates. Over a timescale of more than 4 weeks, independent of the initial surface-to-volume ratio, a semipermeable membrane is fully inflated (relaxation flow) or has reached its steady-state configuration (shear flows).

Under strong confinement we show that water permeation can be amplified on a timescale of a few seconds as a semipermeable inextensible membrane is squeezed through a closely fit channel and a contracting channel. As a semipermeable inextensible membrane goes through a long closely fit channel, we observe loss of water at a constant rate, and the longer the channel the more the loss of water. In the case of a contracting channel, we find that both permeability and the pressure gradient across the slit must be sufficiently large for a successful passage. Throughout these simulations the membrane tension is below the threshold for membrane poration. Thus we expect the continuum membrane theory to well capture the vesicle hydrodynamics, and our simulation results shed light on the configuration and timescales needed to observe the effects of permeability on vesicle hydrodynamics under confinement.

For each of the cases in Sec. IV and Sec. V, we examine the contribution of the permeating flux from membrane tension and membrane bending forces. In free space, we find that both membrane forces contribute comparably in the simulations. As the vesicle hydrodynamics reaches an equilibrium, the two contributions add to zero as the permeating flux integrates to zero rate of change of the reduced area. Under strong confinement, however, we find the membrane tension to contribute much more to the permeating flux than the membrane bending. For a vesicle going through a closely fit channel the maximum flow velocity is $U_{\max} = 1000\mu$m/s is chosen to match

the experimental conditions. Such a large flow velocity contributes to large membrane tension, and thus reducing the timescale for change in water content. For a vesicle going through a contracting channel, we used a smaller $U_{\max}$ than in the experiments (where the three-dimensional channel contracts in both cross-stream directions) to examine the effect of membrane permeability. We find that, due to the strong confinement, the membrane tension still dominates the membrane bending in contributing to the permeating flux as in the closely fit channel.

Cells exhibit a dynamic volume-to-surface ratio in many physiological processes, such as cell migration in confined microenvironments [11,59], dialysis [60], cell desiccation [33], cell division [61], and apoptosis [62]. While osmotic stress is more effective and efficient than mechanical stress in contributing to change in cellular volume, our results suggest that the water permeation due to the capillary pressure may be non-negligible over long times or under strong confinement in simple configurations. To examine if this is the case in the physiological processes, we are currently examining the combined effects of osmotic and mechanical stresses on water permeation in the small Peclet number limit, which is relevant to cellular migration in the presence of both confinement and a solute gradient [11] and has been studied numerically by Jaeger *et al.* [63].

In the literature studies of two-dimensional vesicle hydrodynamics revealed salient features that are also observed in three dimensions, such as a vesicle in shear flow [64,65]. Even though quantitative connection to experimental observation requires some adjustment, results from simulating two-dimensional vesicle hydrodynamics can be insightful for the full three-dimensional simulations of a semipermeable vesicle that we are currently undertaking.

ACKNOWLEDGMENTS

We thank H. A. Stone, M. J. Shelley, P. M. Vlahovska, C. Misbah, M. Abkarian, S. Shin, and S. K. Veerapaneni for discussions. B.Q. acknowledges support from the Simons Foundation, Mathematics and Physical Sciences-Collaboration Grants for Mathematicians, Award No. 527139. Y.-N.Y. acknowledges support from NSF (Grants No. DMS 1614863 and No. DMS 195160) and Flatiron Institute, part of Simons Foundation.

[1] C. Cadart, L. Venkova, P. Recho, M. C. Lagomarsino, and M. Piel, The physics of cell-size regulation across timescales, Nat. Phys. **15**, 993 (2019).

[2] B. Alberts, A. Johnson, J. Lewis, D. Morgan, M. Raff, K. Roberts, and P. Walter, *Molecular Biology of the Cell* (Garland Science, New York, 2015), Chap. 9.

[3] B. Yang, T. Ma, and A. S. Verkman, Erythrocyte water permeability and renal function in double knockout mice lacking aquaporin-1 and aquaporin-3, J. Biol. Chem. **276**, 624 (2001).

[4] J. Sugie, M. Intaglietta, and L. A. Sung, Water transport and homeostasis as a major function of erythrocytes, Am. J. Physiol. Heart Circ. Physiol. **314**, H1098 (2018).

[5] S. Saadoun, M. C. Papadopoulos, H. Watanabe, D. Yan, G. T. Manley, and A. S. Verkman, Involvement of aquaporin-4 in astroglial cell migration and glial scar formation, J. Cell Sci. **118**, 5691 (2005).

[6] A. S. Verkman, M. Hara-Chikuma, and M. Papadopoulos, Aquaporins—New players in cancer biology, J. Mol. Med. **86**, 523 (2008).

[7] A. Berthaud, F. Quemeneur, M. Deforet, P. Bassereau, F. Brochard-Wyart, and S. Mangenot, Spreading of porous vesicles subjected to osmotic shocks: The role of aquaporins, Soft Matter **12**, 1601 (2016).

[8] K. Keren, Cell motility: The integrating role of the plasma membrane, Eur. Biophys. J. **40**, 1013 (2011).

[9] A. Taloni, E. Kardash, O. U. Salman, L. Truskinovsky, S. Zapperi, and C. A. M. La Porta, Volume Changes During Active Shape Fluctuations in Cells, Phys. Rev. Lett. **114**, 208101 (2015).

[10] H. Jiang and S. X. Sun, Cellular pressure and volume regulation and implications for cell mechanics, Biophys. J. **105**, 609 (2013).

[11] K. M. Stroka, H. Jiang, S.-H. Chen, Z. Tong, D. Wirtz, and S. X. Sun, Water permeation drives tumor cell migration in confined microenvironments, Cell **157**, 611 (2014).

[12] Y. Li, Y. Mori, and S. X. Sun, Flow-Driven Cell Migration Under External Electric Fields, Phys. Rev. Lett. **115**, 268101 (2015).
[13] L. Yao and Y. Mori, A numerical method for osmotic water flow and solute diffusion with deformable membrane boundaries in two spatial dimension, J. Comput. Phys. **350**, 728 (2017).
[14] J. Wan, W. D. Ristenpart, and H. A. Stone, Dynamics of shear-induced ATP release from red blood cells, Proc. Natl. Acad. Sci. USA **105**, 16432 (2008).
[15] A. M. Forsyth, J. Wan, P. D. Owrutsky, M. Abkarian, and H. A. Stone, Multiscale approach to link red blood cell dynamics, shear viscosity, and ATP release, Proc. Nat. Acad. Sci. USA **108**, 10986 (2011).
[16] S. Russell-Puleri, N. G. dela Paz, D. Adams, M. Chattopadhyay, L. Cancel, E. Ebong, A. W. Orr, J. A. Frangos, and J. M. Tarbell, Fluid shear stress induces upregulation of COX-2 and PGI2 release in endothelial cells via a pathway involving PECAM-1, PI3K, FAK, and p38, Am. J. Physiol. Heart Circ. Physiol. **312**, H485 (2016).
[17] H. Zhang, Z. Shen, B. Hogan, A. I. Barakat, and C. Misbah, ATP release by red blood cells under flow: Model and simulations, Biophys. J. **115**, 2218 (2018).
[18] E. Gordon, L. Schimmel, and M. Frye, The importance of mechanical forces for *in vitro* endothelial cell biology, Front. Physiol. **11**, 684 (2020).
[19] A. Harman, M. Bertrand, and B. Joos, Deformation and rupture of vesicles confined in narrow channels, Can. J. Phys. **95**, 916 (2017).
[20] M. Razizadeh, M. Nikfar, R. Paul, and Y. Liu, Coarse-grained modeling of pore dynamics on the red blood cell membrane under large deformations, Biophys. J. **119**, 471 (2020).
[21] D. A. T. Dick, The permeability coefficient of water in the cell membrane and the diffusion doefficient in the cell interior, J. Theoret. Biol. **7**, 504 (1964).
[22] R. Fettiplace and D. A. Haydonn, Water permeabilitty of lipid membranes, Physiol. Rev. **60**, 510 (1980).
[23] D. W. Deamer and J. Bramhall, Permeability of lipid bilayers to water and ionic solutes, Chem. Phys. Lipids **40**, 167 (1986).
[24] A. Grafmueller, Multiscale (re)modeling of lipid bilayer membranes, Adv. Biomem. Lipid Self-Assemb. **30**, 1 (2019).
[25] T. E. Thompson and C. Huang, The water permeability of lipid bilayer membranes, Ann. N. Y. Acad. Sci. **137**, 740 (1966).
[26] B. Ugarte-Uribe, A. J. Garcia-Saez, and M. M. A. E. Claessens, Membrane permeability measurements, in *The Giant Vesicle Book*, edited by R. Dimova and C. Marques (CRC Press, Boca Raton, FL, 2019).
[27] T. Bhatia, T. Robinson, and R. Dimova, Membrane permeability to water measured by microfluidic trapping of giant vesicles, Soft Matter **16**, 7359 (2020).
[28] K. Olbrich, W. Rawicz, D. Needham, and E. Evans, Water permeability and mechanical strength of polyunsaturated lipid bilayers, Biophys. J. **79**, 321 (2000).
[29] S.-J. Marrink and H. J. C. Berendsen, Simulation of water transport through a lipid membrane, J. Phys. Chem. **98**, 4155 (1994).
[30] K. Oglecka, P. Rangamani, Bo Liedberg, R. S. Kraut, and A. N. Parikh, Oscillatory phase separation in giant lipid vesicles induced by transmembrane osmotic differentials, eLife **3**, e03695 (2014).
[31] C. Vanhille-Campos and A. Šarić, Modelling the dynamics of vesicle reshaping and scission under osmotic shocks, Soft Matter **17**, 3798 (2021).
[32] T. Bhatia, S. Christ, J. Steinkuhler, R. Dimova, and R. Lipowsky, Simple sugars shape giant vesicles into multispheres with many membrane necks, Soft Matter **16**, 1246 (2020).
[33] C. J. Vogl, M. J. Miksis, S. H. Davis, and D. Salac, The effect of glass-forming sugars on vesicle morphology and water distribution during drying, J. R. Soc., Interface **11**, 20140646 (2014).
[34] C. Minetti, N. Callens, G. Coupier, T. Podgorski, and F. Dubois, Fast measuremennts of concentration profiles inside deformable objects in microflows with reduced spatial coherence digital holography, Appl. Opt. **47**, 5305 (2008).
[35] B. Quaife and G. Biros, High-volume fraction simulations of two-dimensional vesicle suspensions, J. Comput. Phys. **274**, 245 (2014).

[36] A. Rahimian, S. K. Veerapaneni, and G. Biros, Dynamic simulation of locally inextensible vesicles suspended in an arbitrary two-dimensional domain, a boundary integral method, J. Comput. Phys. **229**, 6466 (2010).
[37] L. Lu, A. Rahimian, and D. Zorin, Contact-aware simulations of particulate Stokesian suspensions, J. Comput. Phys. **347**, 160 (2017).
[38] V. Shahin, I. U. Kouzel, G. Rosso, and I. Liashkovich, Nuclear envelop permeability barrier as a fast-response intracellular mechanostat, Adv. Sci. **6**, 1900709 (2019).
[39] J. G. Wijmans, S. Nakao, and C. A. Smolders, Flux limitation in ultrafiltration: Osmotic pressure model and gel layer model, J. Membr. Sci. **20**, 115 (1984).
[40] S. K. Veerapaneni, R. Raj, G. Biros, and P. K. Purohit, Analytical and numerical solutions for shapes of quiescent two-dimensional vesicles, Int. J. Non Linear Mech. **44**, 257 (2009).
[41] R. J. Ryham, On the viscous flows of leak-out and spherical cap natation, J. Fluid Mech. **836**, 502 (2018).
[42] M.-C. Lai, Y.-H. Tseng, and H. Huang, An immersed boundary method for interfacial flows with insoluble surfactant, J. Comput. Phys. **227**, 7279 (2008).
[43] B. K. Alpert, Hybrid Gauss-trapezoidal quadrature rules, SIAM J. Sci. Comput. **20**, 1551 (1999).
[44] B. Quaife and G. Biros, Adaptive time stepping for vesicle simulations, J. Comput. Phys. **306**, 478 (2016).
[45] S. K. Veerapaneni, D. Gueyffier, D. Zorin, and G. Biros, A boundary integral method for simulating the dynamics of inextensible vesicles suspended in a viscous fluid in 2D, J. Comput. Phys. **228**, 2334 (2009).
[46] B. Kaoui, G. Biros, and C. Misbah, Why do Red Blood Cells Have Asymmetric Shapes Even in a Symmetric Flow? Phys. Rev. Lett. **103**, 188101 (2009).
[47] M. Abkarian and A. Viallat, Dynamics of vesicles in a wall-bounded shear flow, Biophys. J. **89**, 1055 (2005).
[48] R. Finken, A. Lamura, U. Seifert, and G. Gompper, Two-dimensional fluctuating vesicles in linear shear flow, Eur. Phys. J. E **25**, 309 (2008).
[49] M. Kraus, W. Wintz, U. Seifert, and R. Lipowsky, Fluid Vesicles in Shear Flow, Phys. Rev. Lett. **77**, 3685 (1996).
[50] G. Danker, P. M. Vlahovska, and C. Misbah, Vesicles in Poiseuille Flow, Phys. Rev. Lett. **102**, 148102 (2009).
[51] C. Pozrikidis, *Boundary Integral and Singularity Methods for Linearized Viscous Flow* (Cambridge University Press, New York, 1992).
[52] M. Abkarian, M. Faivre, and H. A. Stone, High-speed microfluidic differential manometer for cellular-scale hydrodynamics, Proc. Natl. Acad. Sci. USA **103**, 538 (2006).
[53] S. H. Au, B. D. Storey, J. C. Moore, Q. Tang, Y.-L. Chen, S. Javaid, A. F. Sarioglu, R. Sullivan, M. W. Madden, R. O'Keefe, D. A. Haber, S. Maheswaran, D. M. Langenau, S. L. Stott, and M. Toner, Clusters of circulating tumor cells traverse capillary-sized vessels, Proc. Natl. Acad. Sci. USA **113**, 4947 (2016).
[54] On Shun Pak, Y.-N. Young, G. R. Marple, S. Veerapaneni, and H. A. Stone, Gating of a mechanosensitive channel due to cellular flows, Proc. Natl. Acad. Sci. USA **112**, 9822 (2015).
[55] T. Wu, Q. Guo, H. Ma, and J. J. Feng, The critical pressure for driving a red blood cell through a contracting microfluidic channel, Theor. Appl. Mech. Lett. **5**, 227 (2015).
[56] A. Sharei, J. Zoldan, A. Adamo, W. Y. Sim, N. Cho, E. Jackson, S. Mao, S. Schneider, M.-J. Han, A. Lytton-Jean, P. A. Basto, S. Jhunjhunwala, J. Lee, R. Langer, and K. F. Jensen, A vector-free microfluidic platform for intracellular delivery, Proc. Natl. Acad. Sci. USA **110**, 2082 (2013).
[57] Z. Y. Luo and B. F. Bai, Solute release from an elastic capsule flowing through a microfluidic channel constriction, Phys. Fluids **31**, 121902 (2019).
[58] H. Lu and Z. Peng, Boundary integral simulations of a red blood cell squeezing through a submicron slit under prescribed inlet and outlet pressures, Phys. Fluids **31**, 031902 (2019).
[59] M. C. Papadopoulos, S. Saadoun, and A. S. Verkman, Aquaporins and cell migration, Eur. J. Physiol. **456**, 693 (2008).
[60] J. Waniewski, Mathematical modeling of fluid and solute transport in hemodialysis and peritoneal dialysis, J. Membr. Sci. **274**, 24 (2006).

[61] P. D. Odermatt, T. P. Miettinen, J. H. Kang, E. Bostan, S. Manalis, K. C. Huang, and F. Chang, Variations of intracellular density during the cell cycle arise from tip-growth regulation in fission yeast, Elife **10**, e64901 (2010).

[62] P. Marchetti, M. Castedo, S. A. Susin, N. Zamzami, T. Hirsch, A. Macho, A. Haeffner, F. Hirsch, M. Geuskens, and G. Kroemer, Mitochondrial permeability transition is a central coordinating event of apoptosis, J. Exp. Med. **184**, 1155 (1996).

[63] M. Jaeger, M. Carin, M. Medale, and G. Tryggvason, The osmotic migration of cells in a solute gradient, Biophys. J. **77**, 1257 (1999).

[64] G. Ghigliotti, T. Biben, and C. Misbah, Rheology of a dilute two-dimensional suspension of vesicles, J. Fluid Mech. **653**, 489 (2010).

[65] D. Agarwal and G. Biros, Stable shapes of three-dimensional vesicles in unconfined and confined poiseuille flow, Phys. Rev. Fluids **5**, 013603 (2020).